CONDENSED MATTER PHYSICS

Bimodal exciton-plasmon light sources controlled by local charge carrier injection

Pablo Merino,[1]*† Anna Rosławska,[1] Christoph Große,[1]‡ Christopher C. Leon,[1] Klaus Kuhnke,[1] Klaus Kern[1,2]

Electrical charges can generate photon emission in nanoscale quantum systems by two independent mechanisms. First, radiative recombination of pairs of oppositely charged carriers generates sharp excitonic lines. Second, coupling between currents and collective charge oscillations results in broad plasmonic bands. Both luminescence modes can be simultaneously generated upon charge carrier injection into thin C_{60} crystallites placed in the plasmonic nanocavity of a scanning tunneling microscope (STM). Using the sharp tip of the STM as a subnanometer-precise local electrode, we show that the two types of electroluminescence are induced by two separate charge transport channels. Holes injected into the valence band promote exciton generation, whereas electrons extracted from the conduction band cause plasmonic luminescence. The different dynamics of the two mechanisms permit controlling their relative contribution in the combined bimodal emission. Exciton recombination prevails for low charge injection rates, whereas plasmon decay outshines for high tunneling currents. The continuous transition between both regimes is described by a rate model characterizing emission dynamics on the nanoscale. Our work provides the basis for developing blended exciton-plasmon light sources with advanced functionalities.

INTRODUCTION

Modern light sources rely on the efficient coupling between charge carriers and electromagnetic fields at length scales at which quantum effects dominate (*1*, *2*). With advancing miniaturization of photonic devices reaching the single-molecule level (*3*–*5*), it is essential to understand how charge injection affects the luminescence mechanisms at the nanoscale (*6*). When the size of optoelectronic devices approaches the limit of a single quantum system, two main electroluminescence mechanisms dominate (*7*). First, radiative decay of electron-hole bound states (excitons) rules the electroluminescence properties of molecules (*8*, *9*), quantum dots (*10*, *11*), and bulk semiconductors (*12*, *13*). Second, coupling between collective oscillations of electrons (plasmons) and free-propagating photons rules the optoelectronic properties of metallic nanoparticles, nanostructures, and nanocavities (*14*–*16*).

The mechanisms behind photon generation by charge carriers and the interplay between charges, excitons, and plasmons are still the subject of ongoing research. When two metallic nanostructures are separated by less than a nanometer, charge carriers can tunnel between them and alter the electromagnetic modes of the associated cavity (*17*). Tunnel junctions to which a sufficiently high bias voltage is applied can emit light due to current-induced plasmon excitation with typical decay times below a picosecond (*18*, *19*). In contrast, excitons formed at biased molecular junctions have significantly longer radiative lifetimes of typically around a nanosecond (*20*). Coincidentally, in a scanning tunneling microscope (STM) tunnel junction operated with picoampere to nanoampere currents, the average time interval between consecutive tunneling charge carriers ranges from nanoseconds to a few picoseconds. Experimental information about the influence of the carrier injection rate on light emission is extremely sparse (*21*). Further in-depth investigation of the role of the injection dynamics on excitons and plasmons is thus crucial to master the optoelectronic mechanisms operating at the atomic scale.

Here, we show that exciton and plasmon generation can be controlled at the scale of individual molecules in C_{60} films. By benefitting from the different dynamics of excitons and plasmons, we are able to electronically tune their luminescence and produce combined photon emission sources, which we term "bimodal." To precisely control the carrier injection rates, we avoid complex nanoparticle device geometries and make use of precision scanning probe microscopy. We use a sharp gold tip acting as an atomically-localized current source and as an optical antenna coupling electromagnetic radiation from the near to the far field. Exploiting the spatial localization and the defined energy of molecular orbitals, we are able to identify the two charge carrier paths responsible for the two components of the bimodal spectrum. Hole injection and charge trapping at defects induce exciton formation and slow radiative decay. Electron transport through inelastic tunneling processes leads to fast energy transfer to plasmon modes of the nanocavity. By varying the vertical distance and the position of the STM tip on the C_{60} surface, we tune the exciton and plasmon contributions in the optical spectrum and demonstrate full control of this bimodal light source.

RESULTS

In Fig. 1A, we present an STM image of a C_{60} film in which the topography has been overlaid with its photon intensity map. Solid C_{60} is a wide-bandgap organic semiconductor, whose valence band (VB) and conduction band (CB) are derived from the lowest unoccupied molecular orbital (LUMO) and the highest occupied molecular orbital (HOMO), respectively. For films with five (or more) monolayers grown on coinage metal surfaces, applying a voltage bias, U, below −2.7 V induces electroluminescence in the visible and near-infrared range (*22*–*24*). This minimum thickness ensures that the top layers of C_{60} being probed are decoupled from the metal. The color scale in Fig. 1A shows the luminescence intensity, P, measured while rastering the STM tip at constant voltage (U = −3 V) and constant current (I = 20 pA). P is the number of

[1]Max Planck Institute for Solid State Research, Heisenbergstraße 1, 70569 Stuttgart, Germany. [2]Institut de Physique, École Polytechnique Fédérale de Lausanne, 1015 Lausanne, Switzerland.
*Present address: Instituto de Ciencia de Materiales de Madrid, Consejo Superior de Investigaciones Científicas, c/Sor Juana Inés de la Cruz 3, E28049 Madrid, Spain.
†Corresponding author. Email: pablo.merino@csic.es
‡Present address: NanoPhotonics Centre, Cavendish Laboratory, University of Cambridge, Cambridge CB3 0HE, UK.

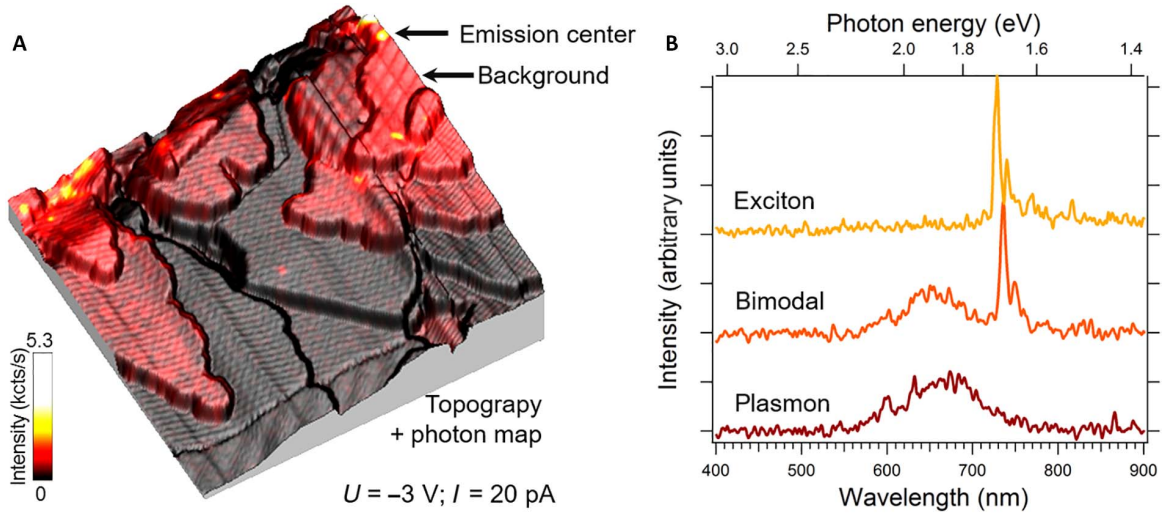

Fig. 1. Overview of STM-induced electroluminescence on C_{60} thin films. (**A**) Pseudo–three-dimensional topographic STM image of the C_{60} surface overlaid with the simultaneously obtained electroluminescence photon map. The C_{60} film exhibits a three-dimensional growth mode on the atomically flat Ag(111) metallic substrate. The top terraces exhibit a homogeneous BKG luminescence (red-colored terraces). In addition, ECs of nanometer extension with different intensities (yellow-colored regions) appear scattered over the surface. Arrows indicate the positions of an EC and a terrace with BKG luminescence. Image size, 150 nm × 150 nm. kcts, kilocounts. (**B**) Typical optical spectra of the exciton (top), bimodal (middle), and plasmon (bottom) luminescence mechanisms. The data were recorded under conditions optimized for each case and were rescaled to make them comparable (U = −3.0 V and I = 100 pA).

photons per second detected by a spectrally integrating photon counter. Most of the C_{60} surface shows very low photon intensities (dark terraces in Fig. 1). In contrast, the C_{60} terraces with a height of five or more monolayers exhibit weak homogeneous luminescence with intensities around 200 to 400 photons/s (red terraces in Fig. 1A). The optical spectrum of this "background" (BKG) luminescence is shown in dark red in Fig. 1B. A broad emission band of ca. 200 nm spectral width demonstrates its plasmonic origin (*6*). Embedded among this BKG luminescence are a few regions of several nanometers in diameter with high photon intensities—up to 5000 detected photons/s. One of these regions marked as an "emission center" (EC) is indicated by an arrow in Fig. 1A. The electroluminescence spectrum obtained when current is injected at this position is shown in orange in Fig. 1B; it is dominated by a sharp line at 740 nm with a vibrational progression extending toward longer wavelengths. In addition, the broadband BKG luminescence is still present in the spectrum, revealing the bimodal character of the electroluminescence. The highly localized sharp spectral line (see yellow spectrum in Fig. 1B) originates from exciton recombination in structural and orientational crystal defects in the C_{60} film (see the Supplementary Materials) (*22*). Only charge injection near these defects results in charge trapping and exciton formation (*20*, *25*). To trace the origin of each type of luminescence, we performed a thorough nanoscale optoelectronic characterization of the films.

We begin our analysis by studying the luminescence from ECs. In our previous work on STM-induced luminescence (STML), we found that crystal defects serve as charge traps and efficient radiative decay regions due to the relaxation of the symmetry-forbidden transition of the lowest energy S_1 exciton of solid C_{60} to the ground state (*22*). Using Hanbury Brown–Twiss interferometry, we moreover revealed that ECs exhibit single photon emission (*20*). Figure 2D shows a photon map of a typical EC recorded in constant height scanning mode. Generally, the photon intensity on ECs is maximum on a central molecule (or group of molecules) and radially decays over nanometer distances (*22*). We imaged the frontier electronic states by recording differential conductance (dI/dU) maps in constant height mode. Figure 2 (A and C) shows the dI/dU measurements that directly represent the local density of states (LDOS) of the CB and the VB, respectively. The LDOS of individual C_{60} molecules at the surface can be imaged with submolecular resolution. Comparing the dI/dU maps and the photon map, we find a positive correlation between the LDOS of the VB (Fig. 2C) and the generation of light on the central molecules of the ECs (Fig. 2D), indicating that hole injection into the VB is responsible for the C_{60} luminescence. This mechanism of excitonic luminescence is illustrated in the energy diagram in Fig. 2E. The sharp spectral lines observed on ECs are the result of hole injection from the STM tip into the hole trap, located energetically close to the VB of C_{60} followed by electron trapping, exciton formation, and subsequent radiative recombination (*20*, *25*).

An equivalent analysis of the BKG luminescence and the comparison between the LDOS and photon maps reveals the second light emission mechanism. A constant height photon map of the BKG light obtained on a C_{60} terrace is shown in Fig. 2I. In contrast to ECs, the photon count rate is comparatively homogeneous across the entire terrace, with an area extending over a few molecules having slightly higher intensities. Once again, the frontier orbital–derived bands are studied in real space. Figure 2 (F and H) shows the surface LDOS of the CB and VB, respectively. For BKG luminescence, the photon map obtained at U = −3.1 V is correlated with the LDOS of the CB. Because C_{60} molecules can exhibit a large variety of orientations at the interface, the LDOS in the CB and VB can vary. C_{60} molecules exhibiting a stronger signal on the dI/dU map measured at U = +1.5 V appear with higher photon intensity at negative bias voltage [see white dashed circles in Fig. 2 (F and I)]. This correlation between the LDOS and the photon map demonstrates that electrons tunneling from the CB to the STM tip are responsible for the BKG luminescence. The mechanism in Fig. 2J illustrates the origin of the broad spectral band observed on the C_{60} surface. At high negative voltages and sufficient film thickness, tip-induced band bending (*26*) pulls the edge of the C_{60} CB below the Fermi level of the surface. Electrons can then be injected from the substrate to the C_{60} CB

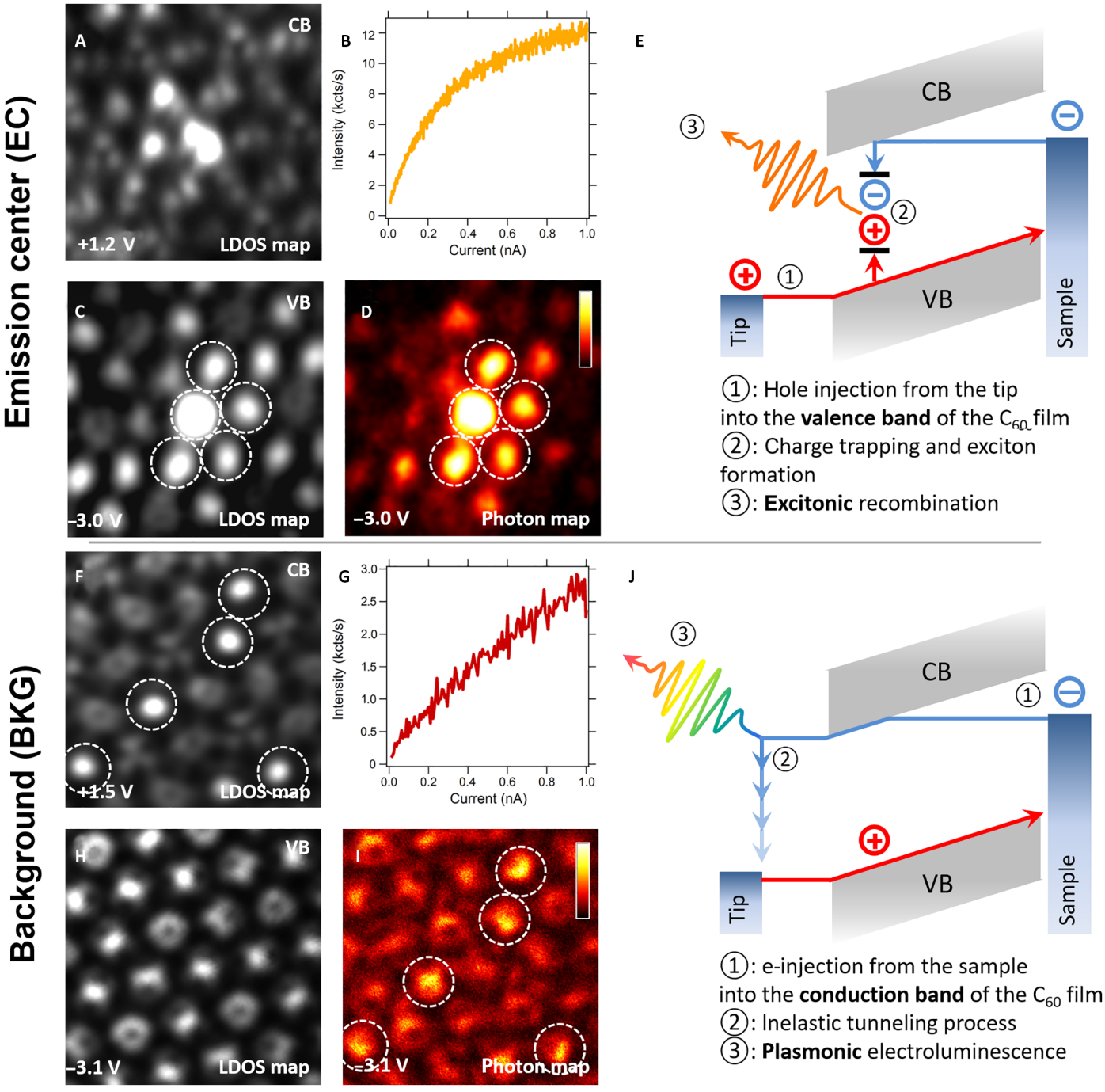

Fig. 2. Characterization of luminescence processes on an EC and on a BKG region. (**A**) LDOS map of the C_{60} CB in the vicinity of an EC on Ag(111), constant height; voltage applied between tip and sample, U = 1.2 V. (**B**) Luminescence versus current function, $P(I)$, measured on an EC, U = −3.0 V. A sublinear dependence is observed. (**C**) LDOS map of the VB in the vicinity of an EC, constant height, U = −3.0 V. (**D**) Constant height photon map of an EC. The molecules with the highest luminescence intensity are marked by white dashed circles to emphasize the similarity with the VB map (C). Color scale, 0 to 16 kcts/s. (**E**) Schematic energy diagram of STM-induced excitonic luminescence on C_{60} films. (**F**) LDOS map of the CB of a C_{60} film on Au(111) with BKG emission, constant height, U = 1.5 V. (**G**) $P(I)$ for BKG luminescence showing a linear dependence of intensity on current, U = −3.0 V. (**H**) LDOS map of the VB of a BKG surface region, constant height, U = −3.1 V. (**I**) Constant height photon map of a BKG surface region. The molecules with the highest luminescence intensity are marked by white dashed circles to emphasize the similarity with the CB map (F). Color scale, 0 to 23 kcts/s. (**J**) Schematic energy diagram of STM-induced plasmonic luminescence on C_{60} films. All STM and photon maps have dimensions of 5 nm × 5 nm.

and tunnel inelastically to the continuum of states in the tip. The energy loss of tunneling electrons can then be transferred to nanocavity plasmon modes leading to light emission in the far field (*27*).

The results show that positive charge carriers (holes) injected and trapped into defect states of the VB control exciton emission, whereas negative charge carriers (electrons) injected from the substrate into the CB and extracted by the tip control plasmonic luminescence. This permits the coexistence of the two electroluminescence mechanisms on some regions of the C_{60} films. In the following, we will show how to control the ratio between both light emission channels by two complementary routes: by varying the real-space injection point and by varying the tunneling current.

The two mechanisms are reflected in the luminescence intensity (P) as a function of tunneling current (I). Figure 2 (B and G) shows $P(I)$ curves obtained on an EC and on BKG light, respectively. They have been measured while ensuring that the tip status remained unchanged for both measurements. As described previously, for low currents, the excitonic photon yield on ECs is higher than that of BKG luminescence. However, the most striking observation is the nonlinearity of the excitonic luminescence intensity as a function of current (Fig. 2B). This behavior is qualitatively different from the linear relation measured for plasmonic luminescence (Fig. 2G). In Fig. 2, we thus show that $P(I)$ curves can be used as a means to distinguish the two involved channels, which is one central finding of our study. The sublinear rise of luminescence intensity on the ECs can be described by a rate constant model for charge injection and recombination extended by exciton-charge annihilation. The quenching of excitons with charges has been found from exciton lifetime measurements as a function of current (*20*). In our model, an EC in the ground state can trap a hole injected from the tip and then capture an electron from the substrate to form an exciton. This exciton can then decay via photon emission or interact with a passing charge and is then quenched (see the Supplementary Materials for details of the model). The excitonic light intensity, P_{ex}, depends on the tunneling current as

$$P_{ex}(I) = \eta \frac{\alpha I}{\alpha I \tau_X + (e + \alpha I \tau_C)\left(1 + \frac{\beta I \tau_X}{e}\right)} \quad (1)$$

where e is the elementary charge, α is the hole trapping efficiency, τ_C is the time for an electron to be captured by a trapped hole, τ_X is the exciton lifetime, β is the exciton-charge annihilation efficiency, and η is the experimental detection probability including all losses occurring between exciton decay and photon detection. Estimating $\tau_X \approx 1$ ns, $\tau_C \approx 1$ ns, and $\eta \approx 10^{-4}$ (see the Supplementary Materials), one can use $P_{ex}(I)$ to fit the trapping (α) and exciton-charge annihilation (β) probabilities. At low current, the average time interval between injected charges, $\tau_{tunnel} = e/I$, is larger than τ_X, and the probability of quenching an exciton by a charge is negligible. Thus, trapping is the dominant factor for luminescence, and hence, α is given by the initial slope of the $P_{ex}(I)$ curve at low current. At currents above 160 pA, τ_{tunnel} is smaller than τ_X. Exciton quenching by charges then becomes important, which leads to a reduction of the exciton lifetime (*20*). In this high current regime, deviations from linearity in $P_{ex}(I)$ are accounted for by a nonzero β value.

We make use of the $P(I)$ dependence to study the smooth transition from the electron-controlled plasmonic luminescence to the hole-controlled excitonic light seen on ECs. In Fig. 3, we present a series of

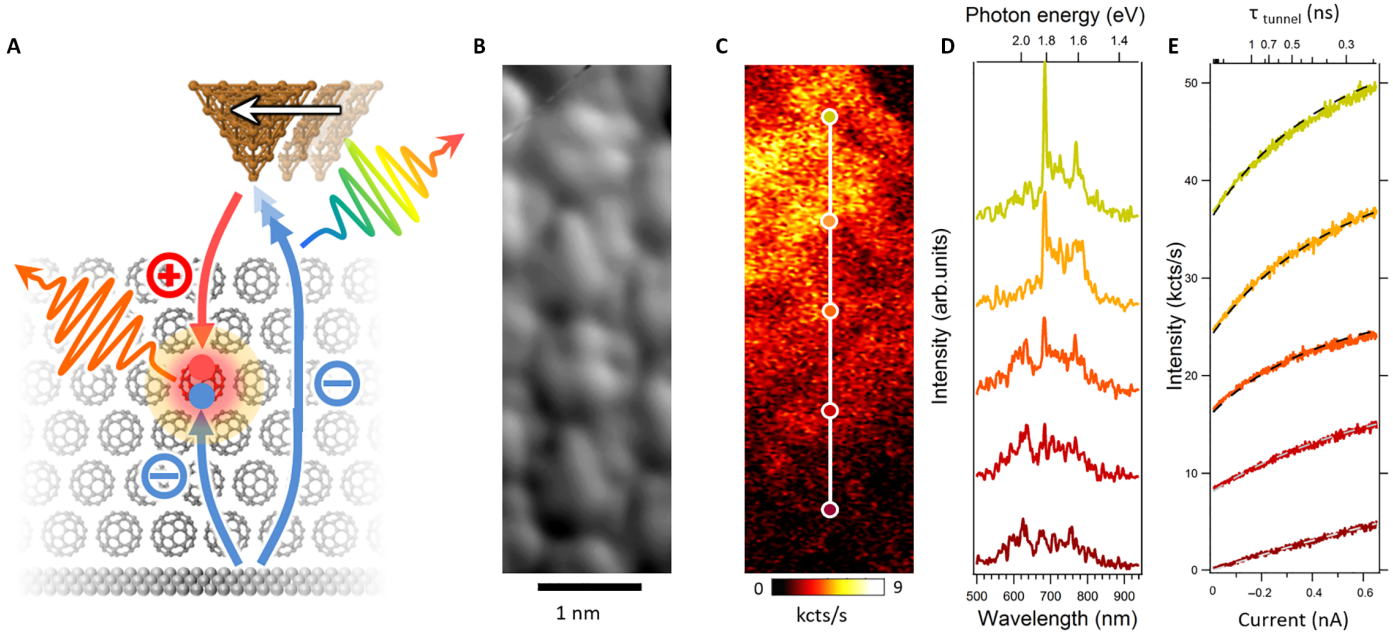

Fig. 3. Bimodal electroluminescence by position-controlled mixing. (**A**) Schematic representation of the experiment presented in (B) to (E). The STM tip approaches an EC laterally at constant current and voltage. (**B**) Constant current STM topography of the investigated surface area of a film grown on Au(111); four C_{60} molecules are imaged 1.5 nm × 4 nm, $U = -3.3$ V, $I = 50$ pA. (**C**) Constant current photon map obtained simultaneously with (B). The five positions of the measurements in (D) and (E) are marked and color-coded. (**D**) Optical spectra obtained on the positions marked in (C). A transition from a broad to a line-dominated spectrum is observed from bottom to top. (**E**) Luminescence versus current function, $P(I)$, measured at the same positions as indicated in (C). The evolution from linear to sublinear behavior correlates with the appearance of the exciton line at 690 nm in the optical spectra presented in (D). Every $P(I)$ measurement in the series is incrementally offset by multiples of 8 kcts/s for clarity. The dashed lines correspond to fits using the model described in the text. For details, see the Supplementary Materials.

measurements performed while laterally approaching an EC. Figure 3A schematically illustrates the experiment. Figure 3 (B and C) shows the constant current topography and photon map along the path toward the EC. Optical spectra and $P(I)$ measurements are presented in Fig. 3 (D and E, respectively). The five measurements in each graph are color-coded (red to yellow), and the surface position of the tip during data acquisition is marked by circles in Fig. 3C. When moving toward an EC, there is an evolution from a broadband spectrum to one dominated by a sharp line. In parallel, the slope of $P(I)$ near $I \approx 0$ increases, and a sublinear behavior develops at higher currents. Both sets of measurements demonstrate achieving a controlled transition from a purely plasmonic luminescence to one dominated by excitonic emission (for details of the fits in Fig. 3E, see the Supplementary Materials). Very recently, Imada *et al.* (*28*) and Zhang *et al.* (*29*) have independently studied the interaction between a plasmonic mode and an individual phthalocyanine (Pc) molecule by STML. They measured the emission spectrum in the vicinity of the Pc molecule adsorbed on NaCl and observed an abrupt change in the luminescence spectra from one dominated by a broad plasmonic band to one dominated by a sharp line within less than 2 Å when approaching the chromophore laterally. Fano-shaped features appeared in the broad plasmonic spectra, which was evidence for energy exchange between plasmons and molecular excitons. The abrupt change to a line-dominated spectrum was attributed to the opening of an excitonic channel on top of the molecules where charge carriers were injected into the highly localized molecular orbitals. In contrast, C_{60} ECs exhibit a continuous transition between the two luminescence mechanisms because positive and negative charge carriers, as well as excitons, can propagate laterally through the spatially extended electronic band structure of the crystalline film. Although plasmon-exciton coupling may still occur in C_{60} films, its manifestation as a Fano feature is not apparent in our experiments. This may be due to the fact that the two emission channels in our study are not phase-coupled because they are driven by two different transport channels.

The different dynamics of the two emission mechanisms present in C_{60} films permit control over light emission simply by varying the injected current. Optical spectra measured at increasingly higher tunneling currents, $I > 1$ nA, exhibit a gradual reduction of the intensity of the sharp line in the spectra. In Fig. 4B, we present a typical measurement of bimodal luminescence on an EC. The relative intensity of the excitonic line at 690 nm decreases when the current is increased and even becomes unobservable for $I = 7.8$ nA. These spectral changes are reproducible and fully reversible with current, ruling out possible tip artifacts or surface modifications (see the Supplementary Materials). In Fig. 4C, we present a $P(I)$ function for currents up to 9 nA. The $P(I)$ curve exhibits three regimes: (i) For low currents, a strong increase in the intensity is observed with the characteristic sublinear behavior; (ii) at a current around 1 nA, the curve has a local maximum and a region of negative slope appears; (iii) around 4 nA, the curve has a local minimum, and a moderate increase in the intensity is observed up to the maximum current applied (red region in Fig. 4C).

DISCUSSION

To model the experiment in Fig. 4C, we introduce a plasmonic BKG luminescence component that is linear in the current

$$P_{\mathrm{pl}}(I) = \frac{\gamma I}{e} \tag{2}$$

with γ being the experimentally observed plasmon quantum yield. The measured luminescence $P(I)$ is then the sum of the excitonic and plasmonic contributions

$$P(I) = P_{\mathrm{ex}}(I) + P_{\mathrm{pl}}(I) \tag{3}$$

Fitting the data with this extended model (orange curve in Fig. 4C) excellently captures the rather complex behavior observed in the experiment. The fit provides the following parameters: a 9% trapping probability ($\alpha \approx 0.09$), a 50% charge annihilation probability ($\beta \approx 0.5$), and a plasmon yield of $\gamma \approx 1.3 \times 10^{-7}$ detected photons per electron. The excitonic (yellow) and plasmonic (red) components of the total

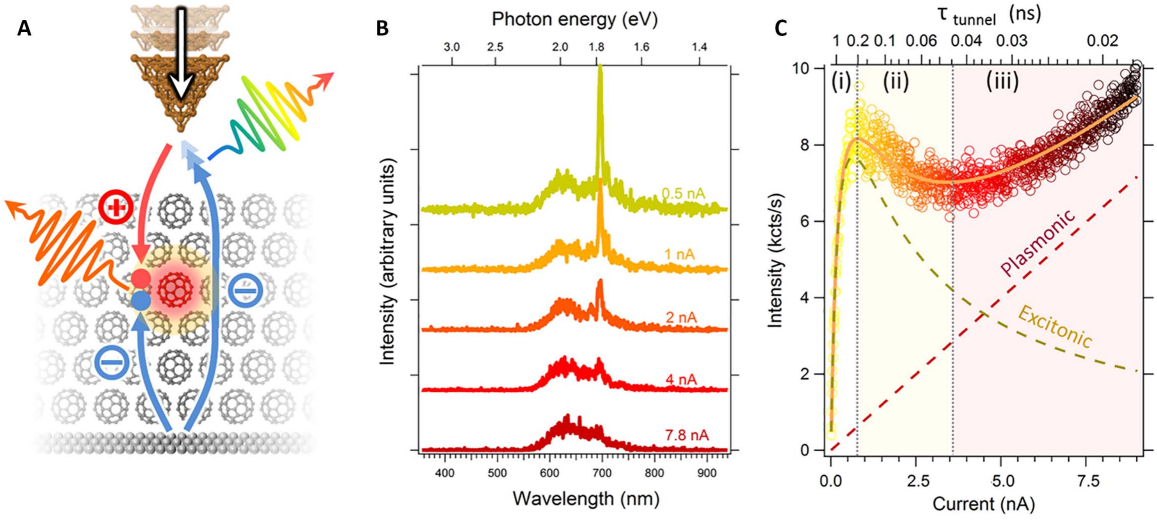

Fig. 4. Control of the bimodal electroluminescence by charge injection dynamics. (**A**) Schematic of the experiment presented in (B) and (C). The STM tip approaches the EC perpendicular to the surface at constant bias voltage, thus increasing the tunnel current, *I*. (**B**) Optical spectra at a fixed surface position and $U = -3$ V for the indicated currents. The accumulation time of each spectrum, *T*, was chosen such that the total injected charge $T \cdot I = 0.05$ μC is constant. (**C**) $P(I)$ measurement extended to high currents with three regimes [(i) to (iii)] discussed in the text.

emission are separately plotted in Fig. 4C. The excitonic component dominates for small injection rates and peaks at $\tau_{tunnel} \approx \tau_X$. The plasmonic component linearly increases with current and dominates for $I >$ 4.5 nA; at these high currents, the long-lived excitons annihilate with current charges before radiative recombination can occur. The competition between exciton annihilation and plasmon excitation is also reflected in the photon maps measured at high injection rates. Figure 5 shows a three-dimensional plot displaying the spatial distribution of the total intensity for increasing currents. At low currents, an EC and a region with BKG luminescence are well distinguished by their distinct brightness (top of the plot). With increasing current, the plasmonic and the excitonic intensities become comparable. When the time between injected charges becomes much shorter than the exciton lifetime, the BKG luminescence outshines the EC emission (bottom of the plot).

We want to stress four points. First, the excitonic component of the bimodal emission does not simply saturate with increasing excitation (that is, charge injection) but rather exhibits a maximum that can be used to obtain an estimate of the exciton lifetime (τ_X). The quenching mechanism of excitons by current injection thus enables practical experimental access to the exciton lifetime without requiring advanced, time-resolved detection schemes. Second, the regime of negative slope of $P_{ex}(I)$, where less light is detected for higher current, may be applicable to realize a NOT-gate coupling between an electric input and a photonic output in future photonic circuitry. Third, we note that a shift of intensity between the two emission channels may not only be due to the different dynamics, as we show here, but also be obtained by tip-induced band bending under appropriate conditions. The latter can contribute to a reduction of the HOMO LDOS and an increase of the LUMO LDOS when the STM tip approaches the film at constant negative bias voltage. For the presented data, however, this mechanism is not dominant. Finally, we implicitly assumed throughout our study that exciton and plasmon emission are basically independent processes. However, because charges pass through the same spatially sharp tunnel junction, one may speculate that close to an EC, both light channels may be time-correlated. We envision future experiments to investigate this point.

In conclusion, we have performed a rigorous nanoscale optoelectronic analysis of the luminescence pathways in C_{60} films. We show by different approaches how the excitonic and plasmonic components can be characterized, separated, and tuned. We described the smooth transition between both regimes and the current dependence by a model that permits the estimation of exciton lifetimes from $P(I)$ curves. Bipolar charge injection on ECs permits us to obtain a quantum system with adjustable electroluminescence properties. The resulting bimodal exciton-plasmon emission may represent a new type of nonclassical light source with mixed properties and open new routes in the field of nanophotonics.

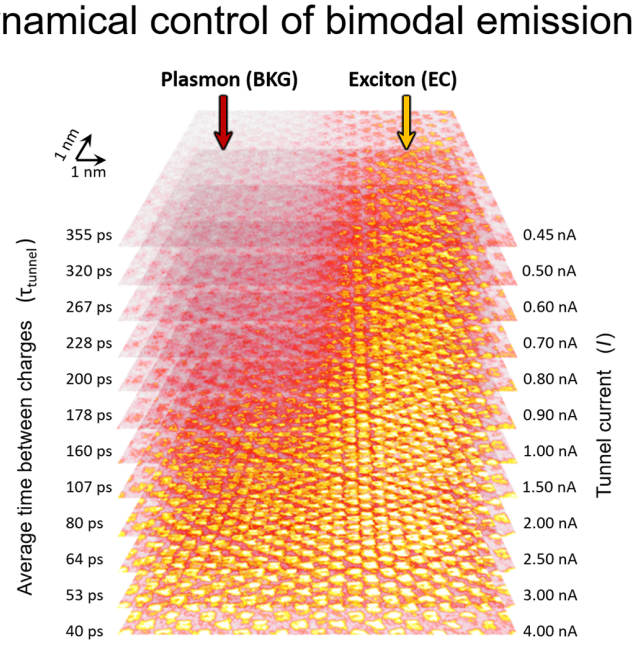

Fig. 5. Spatial distribution and dynamic control of plasmon and exciton emission. Photon maps (13.7 nm × 9.3 nm, $U = -3$ V) of a flat C_{60} terrace on Au(111) containing an EC and a region with BKG luminescence. The constant current maps are stacked as layers on top of each other in a three-dimensional presentation. The current and the corresponding average time between charges are indicated for every layer (scales on the left and right sides, respectively). At injection rates faster than 100 ps, the plasmonic and the excitonic intensities become comparable, and the EC cannot be distinguished from the BKG. All photon maps share the same color scale ranging from 0 to 10 kcts/s.

MATERIALS AND METHODS

Sample fabrication

The C_{60} films were grown on single-crystal metal substrates by molecular evaporation from a Knudsen cell kept at 850 K. The Ag(111) and Au(111) surfaces were previously cleaned in ultrahigh vacuum (UHV) ($<10^{-11}$ mbar) by repeated cycles of Ar^+ sputtering and annealing. The samples were prepared at room temperature and later transferred in situ into the low-temperature STM.

Scanning tunneling microscope

All experiments were performed in a home-built STM operating at 4.2 K with optical access to the tip from three directions (*30*). Light originating from the tunnel junction was collimated on each side by a lens and guided by mirrors and windows along separate pathways to detectors outside the UHV chamber. All detectors operated under ambient conditions. The spectrometer used was an Acton SP 300i with a 150 line/mm blazed (500 nm) grating coupled to a Peltier-cooled intensified charge-coupled device camera. Two single-photon counting avalanche photodiodes (PerkinElmer single-photon counting module, SPCM-AQRH 14) were used to detect the spectrally integrated light intensity. The dark count rate of the detectors was <100 counts/s. Differential conductance (dI/dU) maps were recorded via standard lock-in technique by modulating the bias voltage (5 mV, 777 Hz). All indicated bias voltages refer to the substrate with respect to the grounded STM tip.

SUPPLEMENTARY MATERIALS

Supplementary material for this article is available at http://advances.sciencemag.org/cgi/content/full/4/5/eaap8349/DC1

section S1. EC and BKG luminescence on the molecular scale
section S2. Evaluating $P_{ex}(I)$ in the three-state rate model that includes exciton-charge annihilation
section S3. Fits of $P(I)$ in Fig. 3
section S4. Reversibility of the current dependence of the exciton-to-plasmon ratio
fig. S1. Topography and light intensity channels of EC and BKG luminescence at the molecular scale.
fig. S2. Scheme of the three-state model.
fig. S3. Fits of $P(I)$ of the curves presented in Fig. 3.
fig. S4. Reversibility of the bimodal light source.

REFERENCES AND NOTES

1. L. Novotny, B. Hecht, *Principles of Nano-Optics* (Cambridge Univ. Press, 2012).
2. E. F. Schubert, J. K. Kim, Solid-state light sources getting smart. *Science* **308**, 1274–1278 (2005).
3. A. Kinkhabwala, Z. Yu, S. Fan, Y. Avlasevich, K. Müllen, W. E. Moerner, Large single-molecule fluorescence enhancements produced by a bowtie nanoantenna. *Nat. Photonics* **3**, 654–657 (2009).
4. P. Anger, P. Bharadwaj, L. Novotny, Enhancement and quenching of single-molecule fluorescence. *Phys. Rev. Lett.* **96**, 113002 (2006).
5. S. Kühn, U. Håkanson, L. Rogobete, V. Sandoghdar, Enhancement of single-molecule fluorescence using a gold nanoparticle as an optical nanoantenna. *Phys. Rev. Lett.* **97**, 017402 (2006).
6. K. Kuhnke, C. Große, P. Merino, K. Kern, Atomic-scale imaging and spectroscopy of electroluminescence at molecular interfaces. *Chem. Rev.* **117**, 5174–5222 (2017).
7. M. Achermann, Exciton–plasmon interactions in metal–semiconductor nanostructures. *J. Phys. Chem. Lett.* **1**, 2837–2843 (2010).
8. M. Nothaft, S. Höhla, F. Jelezko, N. Frühauf, J. Pflaum, J. Wrachtrup, Electrically driven photon antibunching from a single molecule at room temperature. *Nat. Commun.* **3**, 628 (2012).
9. H. Imada, K. Miwa, M. Imai-Imada, S. Kawahara, K. Kimura, Y. Kim, Real-space investigation of energy transfer in heterogeneous molecular dimers. *Nature* **538**, 364–367 (2016).
10. Z. Yuan, B. E. Kardynal, R. M. Stevenson, A. J. Shields, C. J. Lobo, K. Cooper, N. S. Beattie, D. A. Ritchie, M. Pepper, Electrically driven single-photon source. *Science* **295**, 102–105 (2002).
11. A. J. Shields, Semiconductor quantum light sources. *Nat. Photonics* **1**, 215–223 (2007).
12. Z. C. Dong, X. L. Zhang, H. Y. Gao, Y. Luo, C. Zhang, L. G. Chen, R. Zhang, X. Tao, Y. Zhang, J. L. Yang, J. G. Hou, Generation of molecular hot electroluminescence by resonant nanocavity plasmons. *Nat. Photonics* **4**, 50–54 (2010).
13. R. Berndt, J. K. Gimzewski, Injection luminescence from CdS(11$\bar{2}$0) studied with scanning tunneling microscopy. *Phys. Rev. B.* **45**, 14095–14099 (1992).
14. A. Yu, S. Li, G. Czap, W. Ho, Tunneling-electron-induced light emission from single gold nanoclusters. *Nano Lett.* **16**, 5433–5436 (2016).
15. K. J. Savage, M. M. Hawkeye, R. Esteban, A. G. Borisov, J. Aizpurua, J. J. Baumberg, Revealing the quantum regime in tunnelling plasmonics. *Nature* **491**, 574–577 (2012).
16. F. Benz, M. K. Schmidt, A. Dreismann, R. Chikkaraddy, Y. Zhang, A. Demetriadou, C. Carnegie, H. Ohadi, B. de Nijs, R. Esteban, J. Aizpurua, J. J. Baumberg, Single-molecule optomechanics in "picocavities". *Science* **354**, 726–729 (2016).
17. W. Zhu, R. Esteban, A. G. Borisov, J. J. Baumberg, P. Nordlander, H. J. Lezec, J. Aizpurua, K. B. Crozier, Quantum mechanical effects in plasmonic structures with subnanometre gaps. *Nat. Commun.* **7**, 11495 (2016).
18. N. L. Schneider, G. Schull, R. Berndt, Optical probe of quantum shot-noise reduction at a single-atom contact. *Phys. Rev. Lett.* **105**, 026601 (2010).
19. J. Lehmann, M. Merschdorf, W. Pfeiffer, A. Thon, S. Voll, G. Gerber, Surface plasmon dynamics in silver nanoparticles studied by femtosecond time-resolved photoemission. *Phys. Rev. Lett.* **85**, 2921–2924 (2000).
20. P. Merino, C. Große, A. Rosławska, K. Kuhnke, K. Kern, Exciton dynamics of C_{60}-based single-photon emitters explored by Hanbury Brown–Twiss scanning tunnelling microscopy. *Nat. Commun.* **6**, 8461 (2015).
21. W. Du, T. Wang, H.-S. Chu, L. Wu, R. Liu, S. Sun, W. K. Phua, L. Wang, N. Tomczak, C. A. Nijhuis, On-chip molecular electronic plasmon sources based on self-assembled monolayer tunnel junctions. *Nat. Photonics* **10**, 274–280 (2016).
22. C. Große, P. Merino, A. Rosławska, O. Gunnarsson, K. Kuhnke, K. Kern, Submolecular electroluminescence mapping of organic semiconductors. *ACS Nano* **11**, 1230–1237 (2017).
23. E. Ćavar, M.-C. Blüm, M. Pivetta, F. Patthey, M. Chergui, W.-D. Schneider, Fluorescence and phosphorescence from Individual C_{60} molecules excited by local electron tunneling. *Phys. Rev. Lett.* **95**, 196102 (2005).
24. F. Rossel, M. Pivetta, W.-D. Schneider, Luminescence experiments on supported molecules with the scanning tunneling microscope. *Surf. Sci. Rep.* **65**, 129–144 (2010).
25. C. Große, O. Gunnarsson, P. Merino, K. Kuhnke, K. Kern, Nanoscale imaging of charge carrier and exciton trapping at structural defects in organic semiconductors. *Nano Lett.* **16**, 2084–2089 (2016).
26. K. Teichmann, M. Wenderoth, S. Loth, R. G. Ulbrich, J. K. Garleff, A. P. Wijnheijmer, P. M. Koenraad, Controlled charge switching on a single donor with a scanning tunneling microscope. *Phys. Rev. Lett.* **101**, 076103 (2008).
27. T. Lutz, C. Große, C. Dette, A. Kabakchiev, F. Schramm, M. Ruben, R. Gutzler, K. Kuhnke, U. Schlickum, K. Kern, Molecular orbital gates for plasmon excitation. *Nano Lett.* **13**, 2846–2850 (2013).
28. H. Imada, K. Miwa, M. Imai-Imada, S. Kawahara, K. Kimura, Y. Kim, Orbital-selective single molecule excitation and spectroscopy based on plasmon-exciton coupling. *Phys. Rev. Lett.* **119**, 013901 (2017).
29. Y. Zhang, Q.-S. Meng, L. Zhang, Y. Luo, Y.-J. Yu, B. Yang, Y. Zhang, R. Esteban, J. Aizpurua, Y. Luo, J.-L. Yang, Z.-C. Dong, J. G. Hou, Sub-nanometre control of the coherent interaction between a single molecule and a plasmonic nanocavity. *Nat. Commun.* **8**, 15225 (2017).
30. K. Kuhnke, A. Kabakchiev, W. Stiepany, F. Zinser, R. Vogelgesang, K. Kern, Versatile optical access to the tunnel gap in a low-temperature scanning tunneling microscope. *Rev. Sci. Instrum.* **81**, 113102 (2010).

Acknowledgments

Funding: P.M. acknowledges the support of the Alexander von Humboldt Foundation. **Author contributions:** P.M., K. Kuhnke, and K. Kern conceived of and designed the research. P.M., A.R., C.G., and C.C.L. performed the experiments. P.M., A.R., and C.G. analyzed the data. All authors contributed to the manuscript. **Competing interests:** The authors declare that they have no competing interests. **Data and materials availability:** All data needed to evaluate the conclusions in the paper are present in the paper and/or the Supplementary Materials. Additional data related to this paper may be requested from the authors.

Submitted 31 August 2017
Accepted 12 April 2018
Published 25 May 2018
10.1126/sciadv.aap8349

Citation: P. Merino, A. Rosławska, C. Große, C. C. Leon, K. Kuhnke, K. Kern, Bimodal exciton-plasmon light sources controlled by local charge carrier injection. *Sci. Adv.* **4**, eaap8349 (2018).